

A dynamically reprogrammable surface with self-evolving shape morphing

<https://doi.org/10.1038/s41586-022-05061-w>

Received: 28 November 2021

Accepted: 1 July 2022

Published online: 21 September 2022



Yun Bai^{1,14}, Heling Wang^{2,3,4,5,6,14}, Yeguang Xue^{2,3,4}, Yuxin Pan¹, Jin-Tae Kim⁷, Xinchen Ni⁷, Tzu-Li Liu⁷, Yiyuan Yang³, Mengdi Han^{7,8}, Yonggang Huang^{2,3,4,7}, John A. Rogers^{2,3,4,7,9,10,11,12} & Xiaoyue Ni^{1,7,13}

Dynamic shape-morphing soft materials systems are ubiquitous in living organisms; they are also of rapidly increasing relevance to emerging technologies in soft machines^{1–3}, flexible electronics^{4,5} and smart medicines⁶. Soft matter equipped with responsive components can switch between designed shapes or structures, but cannot support the types of dynamic morphing capabilities needed to reproduce natural, continuous processes of interest for many applications^{7–24}. Challenges lie in the development of schemes to reprogram target shapes after fabrication, especially when complexities associated with the operating physics and disturbances from the environment can stop the use of deterministic theoretical models to guide inverse design and control strategies^{25–30}. Here we present a mechanical metasurface constructed from a matrix of filamentary metal traces, driven by reprogrammable, distributed Lorentz forces that follow from the passage of electrical currents in the presence of a static magnetic field. The resulting system demonstrates complex, dynamic morphing capabilities with response times within 0.1 second. Implementing an *in situ* stereo-imaging feedback strategy with a digitally controlled actuation scheme guided by an optimization algorithm yields surfaces that can follow a self-evolving inverse design to morph into a wide range of three-dimensional target shapes with high precision, including an ability to morph against extrinsic or intrinsic perturbations. These concepts support a data-driven approach to the design of dynamic soft matter, with many unique characteristics.

Soft matter that can dynamically reconfigure its shape upon interactions with environment or perceptions of information is thriving³¹. Pioneering studies rely on an exploitation of responsive materials (for example, liquid crystal elastomers^{8,9}, dielectric elastomers¹⁰, responsive hydrogels^{11–13} and others¹⁴) and multimaterial structures^{7,15} to enable large deformation, but face challenges in implementing fast control to refined structures. The design of a shape-morphing process usually requires a prerequisite modelling effort to be programmed into the fabrication process, and this is therefore hard to reprogram on-the-fly (for example, 3D printing^{7,11,19,24,30}, magnetization^{19,32}, laser or wafer-jet cutting^{26,27,33}, and mechanical buckling²⁵). The desire to shift shapes among a number of configurations invites investigations of various architectures and programmable stimuli (for example, temperature⁸, light^{34,35}, magnetic field^{20,36}, electric field¹⁰ and Lorentz-force actuation^{22,23,37}). Traditional inverse design of the input–output relationships in the resulting non-linear and high-dimensional system can, however, lead to difficulties in establishing analytical solutions or problems of

high computational costs. Also, existing computer-aided methods usually leave the inclusion of imperfections, damages or coupling between the system and the unforeseen environment. Incorporating instant feedback is necessary for the morphing process to see the deployment scheme to precisely account for specific, multifunctional or time-varying requirements³⁸.

Programmable electromagnetic actuation

A materials architecture consisting of a mesh of optimized, planar conductive features operating in a magnetic field and with programmable control over distributions of electrical current, as introduced here, presents an intriguing set of opportunities. The metasurface takes the form of interconnected, serpentine-shaped beams that consist of a thin conductive layer of gold (Au, thickness $h_{\text{Au}} = 0.3 \mu\text{m}$, width $b_{\text{Au}} = 130 \mu\text{m}$) encapsulated by polyimide (PI, thickness $h_{\text{PI}} = 7.5 \mu\text{m}$, width $b_{\text{PI}} = 160 \mu\text{m}$) (see Methods section ‘Sample fabrication’, Supplementary Fig. 1 and

¹Department of Mechanical Engineering and Materials Science, Duke University, Durham, NC, USA. ²Department of Civil and Environmental Engineering, Northwestern University, Evanston, IL, USA. ³Department of Mechanical Engineering, Northwestern University, Evanston, IL, USA. ⁴Department of Materials Science and Engineering, Northwestern University, Evanston, IL, USA.

⁵Laboratory of Flexible Electronics Technology, Tsinghua University, Beijing, China. ⁶Institute of Flexible Electronics Technology of THU Jiaxing, Zhejiang, China. ⁷Querrey Simpson Institute for Bioelectronics, Northwestern University, Evanston, IL, USA. ⁸Department of Biomedical Engineering, College of Future Technology, Peking University, Beijing, China. ⁹Department of Biomedical Engineering, Northwestern University, Evanston, IL, USA. ¹⁰Department of Neurological Surgery, Feinberg School of Medicine, Northwestern University, Chicago, IL, USA. ¹¹Department of Chemistry, Northwestern University, Evanston, IL, USA. ¹²Department of Electrical and Computer Engineering, Northwestern University, Evanston, IL, USA. ¹³Department of Biostatistics and Bioinformatics, Duke University, Durham, NC, USA. ¹⁴These authors contributed equally: Yun Bai, Heling Wang. [✉]e-mail: helingwang1@gmail.com; y-huang@northwestern.edu; jrogers@northwestern.edu; xiaoyue.ni@duke.edu

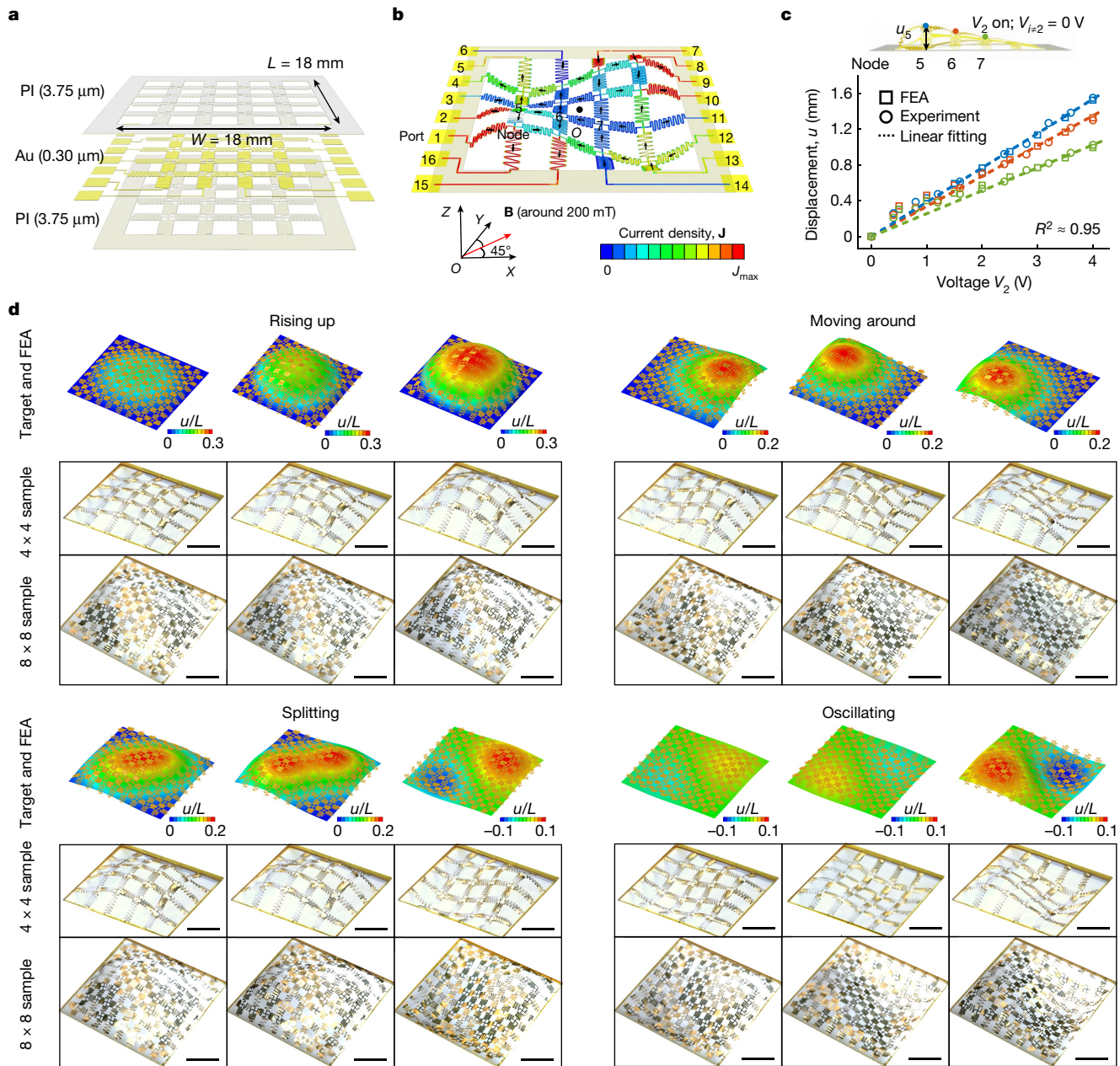


Fig. 1 | Mechanical metasurfaces driven by reprogrammable electromagnetic actuation. **a**, Schematic illustration (enlarged view) of a representative square mesh sample constructed from the serpentine beams consisting of thin PI and Au layers. **b**, Schematic illustration of a 4 × 4 sample placed in a magnetic field (in-plane with the sample in a diagonal direction). Portal voltages define the current density distribution (\mathbf{J}) in the sample and hence control the local Lorentz-force actuation. **c**, FEA provides a linear-model

approximation of the nodal displacement in response to the portal voltage input for the 4 × 4 sample. Experimental characterization using a side camera agrees with the FEA prediction. **d**, FEA and experimental results of a 4 × 4 and 8 × 8 sample morphing into four target abstract shape-shifting processes with control of the instantaneous velocity and acceleration of the dynamics. Scale bars, 5 mm.

Supplementary Note 1 for details). The intersections of the beams form an $N \times M$ mesh as shown in Fig. 1a ($N = M = 4$, sample size $L = W = 18.0$ mm, column and row serpentine beam length $L_{N/M} = 3.60$ mm). A tailored design ensures sufficiently large, fast and reversible out-of-plane deformation ($u/L \approx 30\%$) (in-plane deformation less than $0.01L$; response time less than 0.07 s) of the serpentine beam, driven by a modest electric current ($I < 27.5$ mA) in an approximately uniform magnetic field \mathbf{B} (magnitude $B = 224 \pm 16$ mT) (see Extended Data Fig. 1, Supplementary Figs. 2–6 and Supplementary Notes 2–5 for details). An analytical model validated by experiment can be used to guide design choices for a tunable electromagnetic response in a broad range of magnetic

field strengths (for example, B reduced to 25 mT; see Extended Data Fig. 2 and Supplementary Note 3.1). Figure 1b shows that independent voltages ($\mathbf{V} = \{V_i\}$) of size $2(N + M)$ applied to the peripheral ports define the distribution of current density (\mathbf{J}) in the conductive network (see Methods section ‘Digital control’ and Supplementary Fig. 7 for details) and therefore control the Lorentz force, $\mathbf{F}_{EM} = \mathbf{J} \times \mathbf{B}$. The spatially distributed actuation $\mathbf{F}_{EM}(\mathbf{J})$ determines the local, out-of-plane (Z direction) deformations ($\mathbf{u} = \{u_i\}$, where u_i is the displacement of the i th node) of the sample in a magnetic field \mathbf{B} aligned with its diagonal, enabling a large set of accessible three-dimensional (3D) shapes from the same precursor structure.

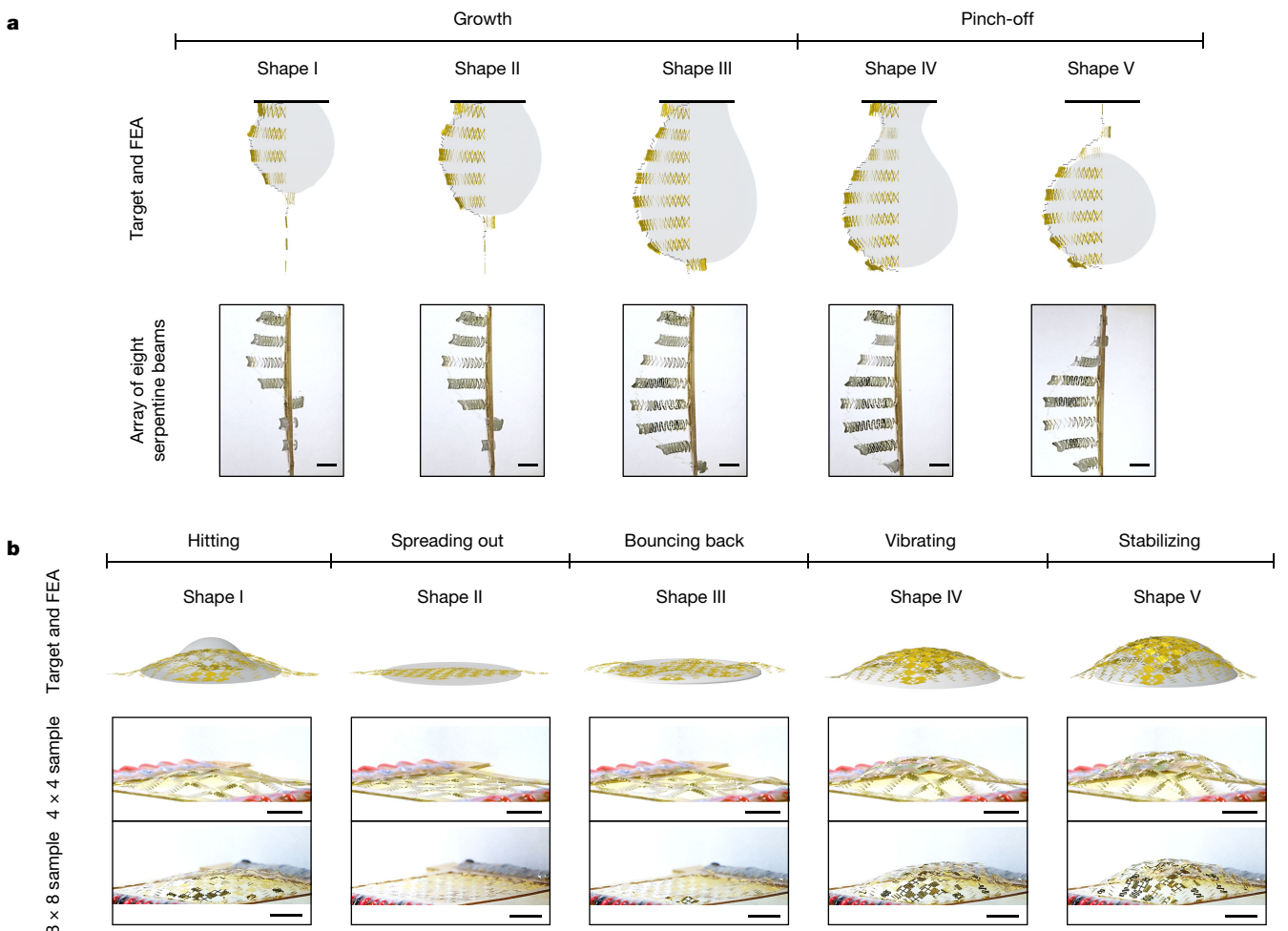


Fig. 2 | Model-driven inverse design of the metasurfaces for dynamic, complex shape morphing. **a**, FEA and experimental results of an array of eight serpentine beams morphing into the growth and pinch-off of a droplet dripping from a nozzle. Scale bars, 2.5 mm. **b**, FEA and experimental results of a 4×4 and an 8×8 sample morphing into the dynamic process of a droplet

hitting a solid surface, spreading out, bouncing back, vibrating and stabilizing. Scale bars, 5 mm. The target shapes in **a** were reconstructed with permission from the images in Fig. 3 in ref.⁴¹ (The American Physical Society). The target shapes in **b** were reconstructed with permission from the frames in supplementary video 1 in ref.⁴² (Elsevier).

Model-driven inverse design

The unusual structure and material design enables the system to adopt an approximate, linearized model, such that the nodal displacement response to the input voltages is as follows:

$$u_i = \sum_{j=1}^{2(N+M)} C_{ij} V_j, \text{ for } i = 1, \dots, N \times M, \quad (1)$$

where the coupling matrix $\mathbf{C} = \{C_{ij}\}$ fully characterizes the electro-magneto-mechanical system. Figure 1c shows the finite-element analysis (FEA) and the experimental characterization of the coupling coefficients C_{ij} for representative nodes in the actuation range of 0–4 V for the 4×4 sample in the magnetic setup. Linear regression of the FEA results predicts \mathbf{C} . The analytical model and the FEA studies, together with experimental validation, provide a scaling law of the coefficients as $C_{ij} \propto (BLH^2 b_{\text{Au}} h_{\text{Au}})/(E_{\text{Pl}} b_{\text{Pl}} h_{\text{Pl}}^3 \rho_{\text{Au}})$ (where H is the serpentine beam width, E_{Pl} is the Pl Young's modulus and ρ_{Au} is the Au electrical conductivity; see Supplementary Figs. 8 and 9 and Supplementary Notes 3.2 and 3.3 for details). Following this linear approximation, a model-driven approach attempts to zero the errors, $e_i(\mathbf{V}) = (u_i(\mathbf{V}) - u_i^*)/L$ (the difference between the output deformation, $u_i(\mathbf{V})$, from the target, u_i^* , normalized by the system size L), to optimize the voltages for the precursor surfaces to deform to a target shape. Given a convex problem with

linear target functions and constraints, a gradient-descent-based algorithm iterates over \mathbf{V} to minimize a loss function, $f(\mathbf{V}) = \sum_i e_i^2(\mathbf{V})$ with a maximum-current constraint (see Methods section 'Optimization algorithm' and Supplementary Note 6 for details). The linearized model-driven approach yields a prediction for \mathbf{V} within 0.01 s. The same approach driven by numerical methods (for example, FEA) without linearization is not possible because of unaffordable computational costs (around 10 days using a workstation with 40-core, 2.4 GHz CPU and 64 GB memory). Figure 1d shows FEA and experimental results of an inverse-designed, continuous shape morphing of a 4×4 and an 8×8 sample ($L = W = 22.4$ mm, $L_{N/M} = 2.48$ mm, see Supplementary Note 7.1 for a detailed discussion of scalability). The process consists of four phases: rising up, moving around, splitting and oscillating, with a prescribed control of the instantaneous velocity and acceleration of the dynamics (Supplementary Video 1, Supplementary Figs. 10–13 and Supplementary Note 8).

In addition to the abstract shapes, the reprogrammable metasurface demonstrates an ability to reproduce dynamic processes in nature that involve a temporal series of complex shapes, provided with the inversely designed current distributions. Figure 2a shows an array of eight serpentine beams ($L = 10.4$ mm, $W = 20.6$ mm, $L_N = 5.2$ mm, $L_M = 2.52$ mm, Supplementary Fig. 14 and Supplementary Note 9) morphing into the two-dimensional profile of a droplet dripping from a nozzle (see Methods section 'Target shapes of the droplets' and Supplementary Fig. 15).

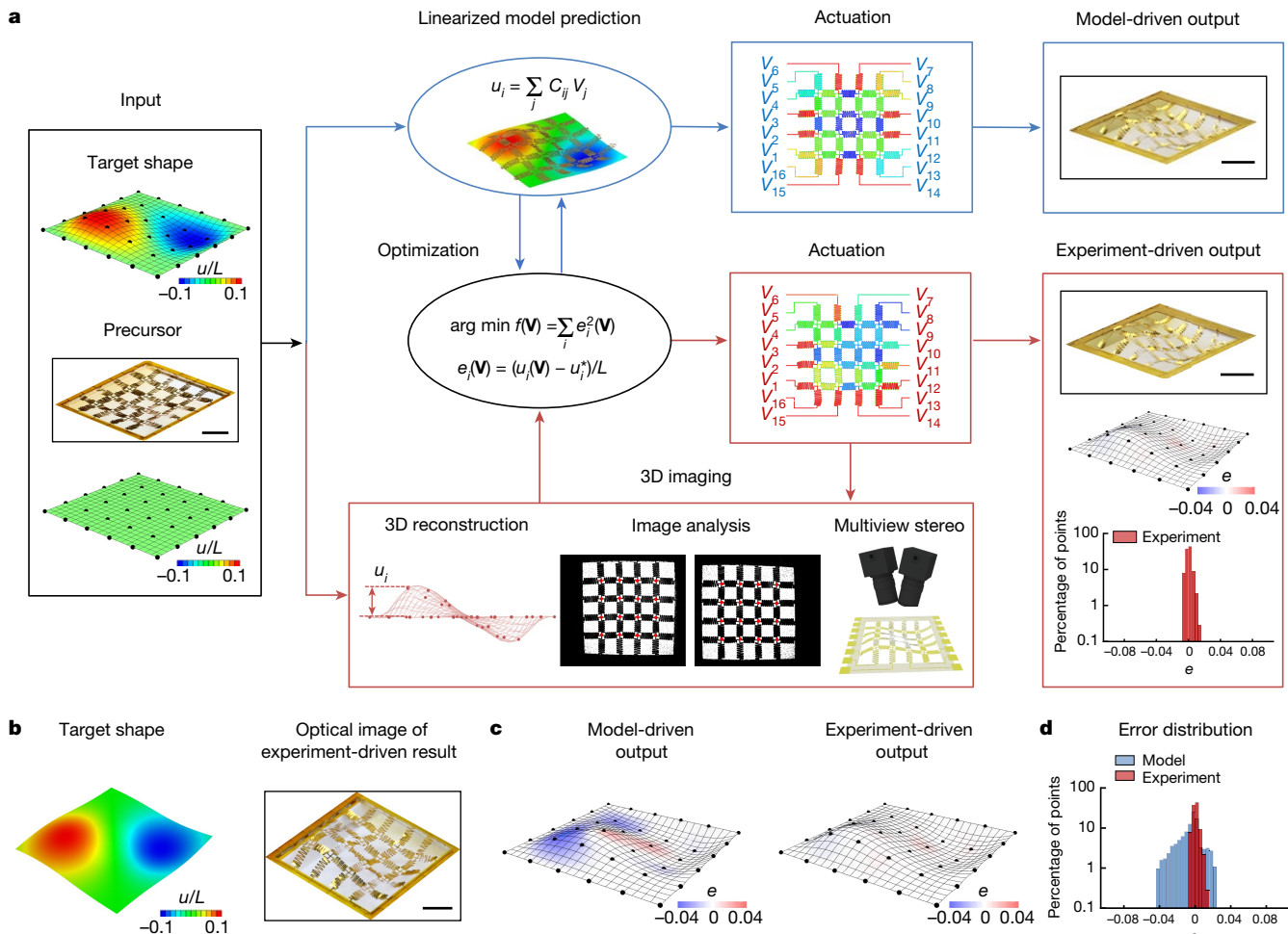


Fig. 3 | The experiment-driven self-evolving process in comparison with the model-driven approach. **a**, A flow diagram of the model-driven inverse design approach (top, blue) and an experiment-driven self-evolving process enabled by in situ 3D imaging feedback and a gradient-descent-based optimization algorithm (bottom, red). **b**, The target abstract shape and optical image of the

experiment-driven morphing result of the 4×4 sample. **c**, 3D reconstructed surfaces overlaid with contour plots of the minimized errors. **d**, Histogram plot of the minimized errors for model-driven and experiment-driven outputs. Scale bars, 5 mm.

Shapes I–III describe the growth of a pendant drop to its critical volume. Shapes IV–V capture the following pinch-off process. Figure 2b presents the 4×4 and 8×8 samples simulating the 3D surface of a droplet falling onto a rigid surface in five stages: hitting the surface, spreading out, bouncing back, vibrating and stabilizing (see Methods section ‘Target shapes of the droplets’, Supplementary Video 2 and Supplementary Figs. 16–19). Numerical analysis further illustrates that the mesh structure can morph into an extensive set of target shapes (Supplementary Figs. 20–27 and Supplementary Notes 8, 10 and 11). Increasing the number of control inputs and introducing a time-varying magnetic field or a field gradient enhance the range of target shapes that can be morphed with sufficient accuracy (Extended Data Fig. 3, Supplementary Figs. 28 and 29, and Supplementary Notes 7 and 12).

The linearized model-driven approach accomplishes an inverse design when a modest error from the non-linearity is tolerable. Extending the model-driven approach to include non-linearity is challenging owing to the large computational expense (Supplementary Note 13) or difficulties in establishing analytical solutions. The open-loop model-based inverse design has constraints on the design space and cannot account for non-ideal factors, such as environmental changes or defects in the sample. The existing limitations motivate the development of sensing feedback for a closed-loop self-evolving inverse design approach.

Experiment-driven self-evolving process

Figure 3a illustrates an experiment-driven process in comparison with the linearized model-driven process. Whereas the model-driven route relies on the presumption of a linear and stationary model, the experimental method takes the in situ measurement of the system output and feeds the difference between the current state and the target state for actuation regulation. In this work, a custom-built stereo-imaging setup using two webcams enables a 3D reconstruction of the nodal displacement at a rate of 30 frames per second, with a displacement resolution of around 0.006 mm and a measurement uncertainty of ± 0.055 mm (see details of 3D imaging in Methods, Supplementary Fig. 30 and Supplementary Note 14). After each update of the actuation (\mathbf{V}), the real-time imaging provides an in situ nodal displacement error analysis. An optimization algorithm (the same one as used in the model-driven approach but wrapping the 3D imaging process) performs the experimental iterations over \mathbf{V} to minimize $f(\mathbf{V})$. For a 4×4 sample morphing into a representative target shape ($f(\mathbf{V} = \mathbf{0}) = 0.05–0.35$), the optimization process takes 5–15 iterations (Extended Data Fig. 4a–c). Each feedback control cycle in the current setup takes around 0.25 s due mainly to the time overhead from the image processing algorithm but this time is ultimately limited by the mechanical response time (which is less than 0.1 s) (Supplementary

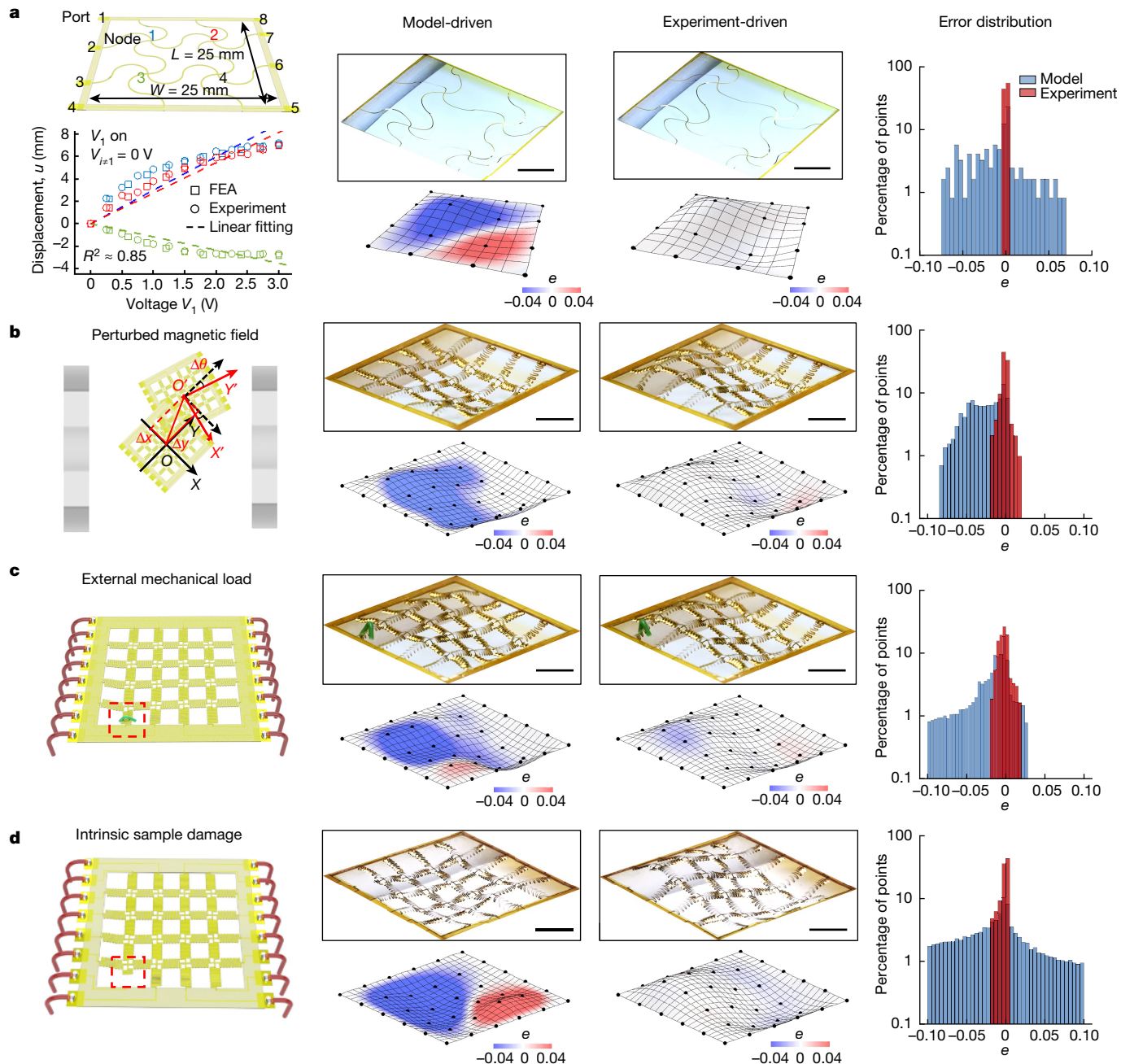


Fig. 4 | Self-evolving shape morphing against extrinsic or intrinsic perturbations. **a–d**, Experimental results of a 2×2 sample (**a**) and a 4×4 sample (**b–d**) morphing into the same target shape (Fig. 3b) via model-driven and experiment-driven processes. A modified serpentine design that amplifies the non-linearity of the voltage-driven deformation (**a**), and the introduction of an extrinsic magnetic perturbation by displacing the sample from the original, centred position ($\Delta x = 8 \text{ mm}$, $\Delta y = 12 \text{ mm}$, $\Delta\theta = 15^\circ$) (**b**), an extrinsic mechanical

perturbation by applying an external mechanical load (around 0.1 g) on a serpentine beam (**c**) and intrinsic damage by cutting one beam open, causing substantial changes in both mechanical and electrical conductivity of the sample (**d**). Left: schematic illustration of the experimental configuration. Middle: optical images and 3D reconstructed surfaces superimposed with an error map. Right: histogram plots of errors. Scale bars, 5 mm .

Table 1 and Supplementary Note 6). A hybrid method, taking a model-driven prediction as the initial input, reduces the number of iterations to around three. The experiment-driven process opens opportunities for the metasurface to self-evolve to target shapes without any previous knowledge of the system (Supplementary Video 3). Figure 3b–d and Extended Data Fig. 5 provide a quantitative comparison between the model-driven and experiment-driven morphing results from the same 4×4 precursor, targeting representative shapes (Supplementary Video 4, Supplementary Figs. 31–33 and Supplementary Note 8). The resulting errors from the model-driven approach

follow a wide (over $\pm 5\%$), mostly skewed distribution (Fig. 3d, considering 441 points from the interpolated 3D surface; Supplementary Note 14). The experiment-driven approach, accounting for the subtle non-linear deviation, yields a relatively narrow ($\pm 2\%$), symmetric error distribution. The dominant sources of errors are the discreteness in the input voltages and the uncertainties associated with the 3D imaging (Extended Data Fig. 6 and Supplementary Note 14). Experimental noise also adds complexity to the error function and, when pronounced, requires global optimization solvers (Extended Data Fig. 4d–f and Supplementary Note 6).

Article

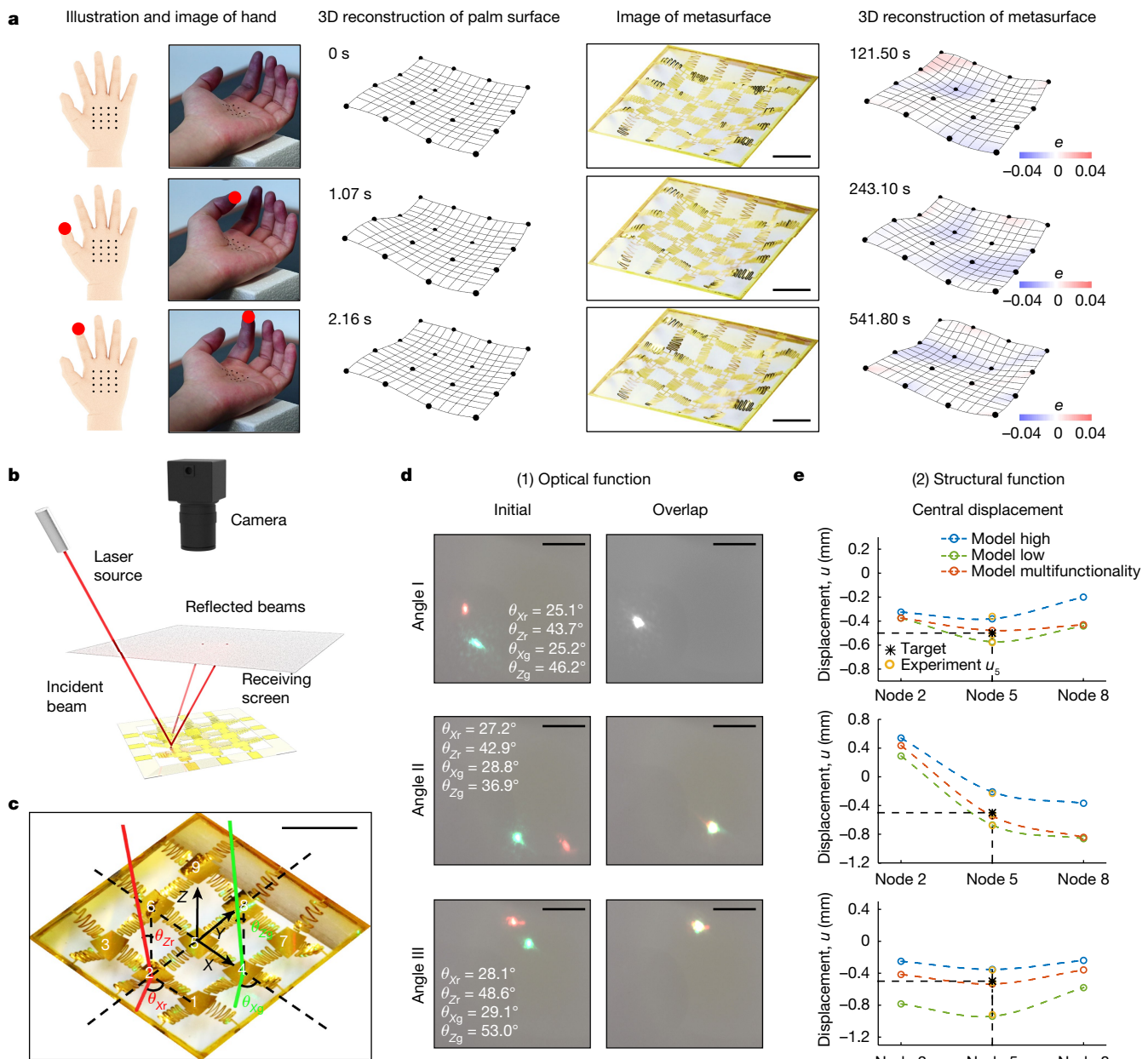


Fig. 5 | Self-evolving shape morphing towards semi-real-time shape learning and multifunctionality. **a**, Morphing results of representative frames from a recording of a hand making eight gestures with different fingers moving. **b**, Schematic illustration of a 3×3 sample with gold patches ($2 \text{ mm} \times 2 \text{ mm}$ in size, $0.3 \mu\text{m}$ in thickness) mounted on the nodes reflecting a laser beam from an incident angle. A top-positioned camera monitors the laser spot projected on a paper screen. **c**, An optical image of a 3×3 sample with nine reflective patches morphing via a hybrid experiment-driven and model-driven process to perform two functions: (1) reflecting and overlapping two laser

beams (red, green) with different incident angles ($[\theta_{x_r}, \theta_{z_r}], [\theta_{x_g}, \theta_{z_g}]$) and (2) achieving the target displacement (-0.5 mm) of the central node (u_s) of the sample. **d**, Imaging of the screen from the camera provides experimental feedback of the distance between the two laser spots. **e**, Model predictions of the displacement profile of the sample (cross-sectional view) when overlapping the laser spots with the highest-possible (blue), lowest-possible (green) and optimized (red) central positions. Ex situ stereo imaging provides 3D reconstructed measurement of the optimized deformation (orange) that validates the in situ model predictions. Scale bars, 5 mm .

The experiment-driven process works as a physical simulation to accommodate appreciable non-linearity without a substantial increase in the computational cost. Figure 4a introduces a 2×2 sample ($L = W = 25.0 \text{ mm}$, $L_{NM} = 10.25 \text{ mm}$) morphing into the same target shape in Fig. 3b. Centred in the same magnetic setup, the sample shows an amplified non-linear mechanical behaviour in response to input voltages due to the reduced arc length of each serpentine beam (Extended Data Fig. 7 and Supplementary Note 15). The model-driven approach based on the assumption of a linear system results in an absolute maximum error of around 8%. The experiment-driven approach achieves a

more accurate morphing result in around 20 iterations with absolute errors below 1%.

Guided by the experiment-driven process, the metasurface can also self-adjust to morph against unknown perturbations. Figure 4b–d shows three representative cases in which a 4×4 sample morphs with perturbed magnetic field, external mechanical load and intrinsic damage, respectively. In all cases, the model-driven approach following the original inverse design results in absolute maximum errors of around 8–10%. In comparison, the experiment-driven approach adapts the shape to reach the target with absolute errors below around 3%, which is

comparable with that of an intact sample (around 2%) (Supplementary Video 5). The boosted accuracy level demonstrates the ‘self-sustained’ morphing ability enabled by the experiment-driven process.

Shape learning and multifunctionality

The adaptive, self-evolving metasurface platform delivers a semi-real-time morphing scheme to learn the continuously evolving surface of a real object. In this experiment, a duplicated stereo-imaging setup measures the displacement of a 4×4 array of markers (with inter-spacing $a_0 = 15$ mm) on the palm (Extended Data Fig. 8a). The optimization acts directly to minimize the displacement difference between the 16 markers and their corresponding nodes in the 4×4 sample. Given continuity, the gradient-descent process takes the last morphing result as the initial state for the next morphing task. This differential method (with the target descent $\Delta f(V) \approx 0.0032$) requires only at most three iterations (approximately 20 s) to reach the optimum. Figure 5a shows the representative frames from a video recording a hand making eight gestures with different fingers moving (see Supplementary Video 6 and Extended Data Fig. 8b,c for complete results of all gestures). All morphing results agree with the target with absolute errors below 2%.

In addition to self-evolving to optimize shapes, the metasurface can self-evolve to optimize functions. Setting multiple target functions drives the optimization towards emergent multifunctionality, with the ability to decouple naturally coupled functions. Figure 5b,c illustrates a scheme in which a 3×3 sample ($L = W = 14.8$ mm, $L_{NM} = 4.06$ mm) with nine reflective gold patches at the nodes attempts to perform an optical and a structural function: (1) reflecting and overlapping two laser beams (red, green) with different incident angles ($[\theta_{xr}, \theta_{zr}], [\theta_{xg}, \theta_{zg}]$) on a receiving screen (Extended Data Fig. 9a) and (2) achieving the target displacement of the central node of the sample. The optimization takes a hybrid strategy combining the model-driven and experiment-driven processes (Supplementary Note 16). While the voltages control the reflected beam paths, a top camera provides imaging feedback of the distances between the beam spots on the screen. The model-driven process predicts the difference between the central nodal displacement and the target. The total loss takes a linear combination of the two errors (Extended Data Fig. 9b and Supplementary Note 16). Figure 5d shows the self-evolving results of three optical configurations with distinctive incident beam angles. Figure 5e shows that the metasurface can morph to overlap the laser spots on the receiving screen with a range of possible shapes (Extended Data Fig. 10a). By enforcing both functions, the sample overlaps the spots and settles its central node to a target displacement. A post analysis through ex situ 3D imaging validates that the final experimental central nodal displacement reaches the target within an error of $\pm 2\%$ (Supplementary Video 7 and Extended Data Fig. 10b).

Discussion

The work presents a reprogrammable metasurface that can precisely and rapidly morph into a wide range of target shapes and dynamic shape processes. The Lorentz-force-driven serpentine mesh construction supports an approximately linear input–output response with easily accessible solutions to the inverse problem. The highly integrable digital–physical interfaces incorporating actuation, sensing and feedback enable an in-loop optimization process to attain model-free solutions when the system deviates from the linear, time-invariant response. The experiment-driven shape-shifting capability addresses theoretical and computational challenges in complex, non-linear systems, bringing new opportunities for physical simulations for a real-time, data-driven inverse design process. Such a scheme enables an autonomous materials platform to promptly change structures, actively explore the design space and responsively reconfigure functionalities. The platform is compatible with the typical materials,

structures and thin-film fabrication techniques used in existing flexible electronics frameworks. It supports optimized choices of materials, geometries, layouts, control systems and magnetic setups for design flexibility and potential scalability, which promises a wide, versatile application scenario in wearable techniques, soft robotics and advanced materials. Many possibilities exist to improve this system, such as incorporating a mechanical locking mechanism (for example, applying phase transition materials^{21,39} or a jamming configuration⁴⁰ could hold the morphed shapes without actuation). Exploring constructions with low in-plane stiffness will enable additional deformation modes of the metasurface (Supplementary Fig. 34). The demonstration of the current modular platform invites higher levels of integration to embed functional materials and components into the morphing matter, to support on-board power sources (supercapacitors), sensors (strain gauges), feedback control mechanisms (analogue devices), computational resources (microcontrollers) and wireless communication capabilities (radios). Using advanced data-driven techniques in the loop (for example, Bayesian optimization, deep learning and reinforcement learning) will enhance the capabilities of self-evolving designs for artificial matter in pursuit of functions or performance inspired by those in their natural counterparts, paving the way for new classes of intelligent materials that adopt spatiotemporally controlled shapes and structures for advanced on-demand functionalities.

Online content

Any methods, additional references, Nature Research reporting summaries, source data, extended data, supplementary information, acknowledgements, peer review information; details of author contributions and competing interests; and statements of data and code availability are available at <https://doi.org/10.1038/s41586-022-05061-w>.

1. Rafsanjani, A., Bertoldi, K. & Studart, A. R. Programming soft robots with flexible mechanical metamaterials. *Sci. Robot.* **4**, eaav7874 (2019).
2. McEvoy, M. A. & Correll, N. Materials that couple sensing, actuation, computation, and communication. *Science* **347**, 1261689 (2015).
3. Morin, S. A. et al. Camouflage and display for soft machines. *Science* **337**, 828–832 (2012).
4. Wang, C., Wang, C., Huang, Z. & Xu, S. Materials and structures toward soft electronics. *Adv. Mater.* **30**, 1801368 (2018).
5. Rogers, J. A., Someya, T. & Huang, Y. Materials and mechanics for stretchable electronics. *Science* **327**, 1603–1607 (2010).
6. Cianchetti, M., Laschi, C., Menciassi, A. & Dario, P. Biomedical applications of soft robotics. *Nat. Rev. Mater.* **3**, 143–153 (2018).
7. Boley, J. W., Rees, W., Lissandrello, C., Horenstein, M. N. & Mahadevan, L. Shape-shifting structured lattices via multimaterial 4D printing. *Proc. Natl. Acad. Sci. USA* **116**, 201908806 (2019).
8. Liu, K., Hacker, F. & Daraio, C. Robotic surfaces with reversible, spatiotemporal control for shape morphing and object manipulation. *Sci. Robot.* **6**, eabf5116 (2021).
9. Guo, Y., Zhang, J., Hu, W., Khan, M. T. A. & Sitti, M. Shape-programmable liquid crystal elastomer structures with arbitrary three-dimensional director fields and geometries. *Nat. Commun.* **12**, 5936 (2021).
10. Hajiesmaili, E. & Clarke, D. R. Reconfigurable shape-morphing dielectric elastomers using spatially varying electric fields. *Nat. Commun.* **10**, 183 (2019).
11. Gladman, A. S., Matsumoto, E. A., Nuzzo, R. G., Mahadevan, L. & Lewis, J. A. Biomimetic 4D printing. *Nat. Mater.* **15**, 413–418 (2016).
12. Yu, C. et al. Electronically programmable, reversible shape change in two-and three-dimensional hydrogel structures. *Adv. Mater.* **25**, 1541–1546 (2013).
13. Zhang, H., Guo, X., Wu, J., Fang, D. & Zhang, Y. Soft mechanical metamaterials with unusual swelling behavior and tunable stress-strain curves. *Sci. Adv.* **4**, eaar8535 (2018).
14. Li, S. et al. Liquid-induced topological transformations of cellular microstructures. *Nature* **592**, 386–391 (2021).
15. Pikul, J. et al. Stretchable surfaces with programmable 3D texture morphing for synthetic camouflaging skins. *Science* **358**, 210–214 (2017).
16. Barnes, M. et al. Reactive 3D printing of shape-programmable liquid crystal elastomer actuators. *ACS Appl. Mater. Interfaces* **12**, 28692–28699 (2020).
17. Ford, M. J. et al. A multifunctional shape-morphing elastomer with liquid metal inclusions. *Proc. Natl. Acad. Sci. USA* **116**, 21438–21444 (2019).
18. Alapan, Y., Karacakol, A. C., Guzelhan, S. N., Isik, I. & Sitti, M. Reprogrammable shape morphing of magnetic soft machines. *Sci. Adv.* **6**, eabc6414 (2020).
19. Kim, Y., Yuk, H., Zhao, R., Chester, S. A. & Zhao, X. Printing ferromagnetic domains for untethered fast-transforming soft materials. *Nature* **558**, 274–279 (2018).
20. Cui, J. et al. Nanomagnetic encoding of shape-morphing micromachines. *Nature* **575**, 164–168 (2019).

21. Ze, Q. et al. Magnetic shape memory polymers with integrated multifunctional shape manipulation. *Adv. Mater.* **32**, 1906657 (2020).
22. Mao, G. et al. Soft electromagnetic actuators. *Sci. Adv.* **6**, eabc0251 (2020).
23. Zhang, F. et al. Rapidly deployable and morphable 3D mesostructures with applications in multimodal biomedical devices. *Proc. Natl Acad. Sci. USA* **118**, e2026414118 (2021).
24. Xia, X. et al. Electrochemically reconfigurable architected materials. *Nature* **573**, 205–213 (2019).
25. Fan, Z. et al. Inverse design strategies for 3D surfaces formed by mechanically guided assembly. *Adv. Mater.* **32**, 1908424 (2020).
26. Choi, G. P., Dudte, L. H. & Mahadevan, L. Programming shape using kirigami tessellations. *Nat. Mater.* **18**, 999–1004 (2019).
27. Bossart, A., Dykstra, D. M., van der Laan, J. & Coulais, C. Oligomodal metamaterials with multifunctional mechanics. *Proc. Natl Acad. Sci. USA* **118**, e2018610118 (2021).
28. Baek, C., Martin, A. G., Poincloux, S., Chen, T. & Reis, P. M. Smooth triaxial weaving with naturally curved ribbons. *Phys. Rev. Lett.* **127**, 104301 (2021).
29. Coulais, C., Sabbadini, A., Vink, F. & van Hecke, M. Multi-step self-guided pathways for shape-changing metamaterials. *Nature* **561**, 512–515 (2018).
30. Guseinov, R., McMahan, C., Pérez, J., Daraio, C. & Bickel, B. Programming temporal morphing of self-actuated shells. *Nat. Commun.* **11**, 237 (2020).
31. Kaspar, C., Ravoo, B. J., van der Wiel, W. G., Wegner, S. V. & Pernice, W. H. P. The rise of intelligent matter. *Nature* **594**, 345–355 (2021).
32. Hu, W., Lum, G. Z., Mastrangeli, M. & Sitti, M. Small-scale soft-bodied robot with multimodal locomotion. *Nature* **554**, 81–85 (2018).
33. Overvelde, J. T., Weaver, J. C., Hoberman, C. & Bertoldi, K. Rational design of reconfigurable prismatic architected materials. *Nature* **541**, 347–352 (2017).
34. Waters, J. T. et al. Twist again: dynamically and reversibly controllable chirality in liquid crystalline elastomer microposts. *Sci. Adv.* **6**, eaay5349 (2020).
35. Wang, Y. et al. Repeatable and reprogrammable shape morphing from photoresponsive gold nanorod/liquid crystal elastomers. *Adv. Mater.* **32**, 2004270 (2020).
36. Xu, C., Yang, Z. & Lum, G. Z. Small-scale magnetic actuators with optimal six degrees-of-freedom programming temporal morphing of self-actuated shells. *Adv. Mater.* **33**, 2100170 (2021).
37. Phelan, M. F. III, Tiriyaki, M. E., Lazovic, J., Gilbert, H. & Sitti, M. Heat-mitigated design and lorentz force-based steering of an MRI-driven microcatheter toward minimally invasive surgery. *Adv. Sci.* **9**, 2105352 (2022).
38. Kotikian, A. et al. Innervated, self-sensing liquid crystal elastomer actuators with closed loop control. *Adv. Mater.* **33**, 2101814 (2021).
39. Wang, X. et al. Freestanding 3D mesostructures, functional devices, and shape-programmable systems based on mechanically induced assembly with shape memory polymers. *Adv. Mater.* **31**, 1805615 (2019).
40. Wang, Y., Li, L., Hofmann, D., Andrade, J. E. & Daraio, C. Structured fabrics with tunable mechanical properties. *Nature* **596**, 238–243 (2021).
41. Zhang, B. et al. Short-term oscillation and falling dynamics for a water drop dripping in quiescent air. *Phys. Rev. Fluids* **4**, 123604 (2019).
42. Tang, C. et al. Dynamics of droplet impact on solid surface with different roughness. *Int. J. Multipiph. Flow* **96**, 56–69 (2017).

Publisher's note Springer Nature remains neutral with regard to jurisdictional claims in published maps and institutional affiliations.

Springer Nature or its licensor holds exclusive rights to this article under a publishing agreement with the author(s) or other rightsholder(s); author self-archiving of the accepted manuscript version of this article is solely governed by the terms of such publishing agreement and applicable law.

© The Author(s), under exclusive licence to Springer Nature Limited 2022

Methods

Sample fabrication

The fabrication process (Supplementary Fig. 1) began with the spin coating of a thin layer of PI (HD Microsystems PI2545, 3.75 μm in thickness) on a silicon wafer with poly(methyl methacrylate) (Microresist 495 A5, 0.08 μm in thickness) as the sacrificial layer. Subsequent lift-off processes patterned the metal electrodes and serpentine connections (Ti/Au, 10 nm/300 nm in thickness). Spin coating another layer of PI (HD Microsystems PI2545, 3.75 μm in thickness) covered the metal pattern. Photolithography and oxygen plasma etching of PI defined the outline of the sample. Undercutting the bottom layer of poly(methyl methacrylate) allowed the transfer of the sample to a water-soluble polyvinyl alcohol tape (3M) from the silicon wafer.

Digital control

The digital control system used (1) pulse-width modulation (PWM) drivers (PCA9685, 16-channel, 12-bit), (2) voltage amplifier circuits (MOSFET, IRF510N, Infineon Tech) and (3) a single-board computer (Raspberry Pi 4) remotely connected to an external computer (Intel NUC, Intel Core i7-8559U CPU@2.70 GHz). The external computer ran the optimization algorithm and sent the updated values of the voltages wirelessly to the single-board computer through Python Socket network programming. The PWM driver received the actuation signals from the single-board computer. Each PWM channel, operated at a frequency of 1,000 Hz, generated an independent voltage in the range of 0–6 V with 12-bit (around 0.0015 V) resolution. The single stage MOSFET provided a reversely linear amplification to the PWM output with a gate voltage, $V_{\text{gs(th)}} = 4 \text{ V}$, and an external power supply, $V_{\text{ex}} = 6 \text{ V}$ (Supplementary Fig. 7).

Optimization algorithm

Sequential least squares programming with a three-point method (SciPy-Python optimize.minimize function) computed the Jacobian matrix in the loop to minimize the loss function $f(\mathbf{V})$. The model-driven approach adopted the same optimization algorithm, with $f(\mathbf{V})$ evaluated by equation (1) and a maximum of around 10,000 iterations. For the experiment-driven approach, a maximum final loss value of 0.005 $f(\mathbf{V} = \mathbf{0})$ and a maximum of 15 iterations set the stopping criteria for the optimization process. Each iteration required $4(N + M) + 2$ function evaluations for an $N \times M$ sample (Supplementary Note 6).

Target shapes of the droplets

The target shapes in Fig. 2a were reconstructed from the images in Fig. 3 in ref.⁴¹. The target shapes in Fig. 2b were reconstructed from frames of the supplementary video in ref.⁴². 3D models of the target shapes were built and rendered using Solidworks (Dassault Systèmes). The target shapes and slow-motion video in Supplementary Video 2 were reconstructed (00:00:15–00:04:23, 0.6× playback) and reproduced from ref.⁴².

3D imaging

The multiview stereo-imaging platform consisted of two cameras (Webcams, ELP, MI5100, 3,840 × 2,160-pixel resolution, 30 frames per second) connected to the external computer taking top-view images of the sample from symmetric angles (Supplementary Fig. 30a). A calibration algorithm (OpenCV-Python calibrateCamera function) applied to a collection of images of a chequerboard (custom-made, 7 × 8 squares, 2 mm × 2 mm per square) returned the camera matrix, distortion coefficients, rotation and translation vectors to correct for the lens distortion of the images (OpenCV-Python undistort function). The nodes of the mesh samples provided a distinguishable geometry for image registration. A template matching algorithm (OpenCV-Python matchTemplate function) returned the locations of the nodes in the images from the two cameras. A perspective projection algorithm (OpenCV-Python reprojectImageTo3D function) transformed the disparity map into the nodal heights in units of pixels. An additional side camera provided ground-truth measurements of the displacement of the discernible nodes and provided a linear-model prediction of the 3D-reconstructed nodal displacement (Supplementary Fig. 30b,c and Supplementary Note 14).

Data availability

All data are contained within the manuscript. Raw data are available from the corresponding authors upon reasonable request.

Code availability

The codes that support the findings of this study are available from the corresponding authors upon reasonable request.

Acknowledgements Y.B., Y.P. and Xiaoyue Ni acknowledge funding support from the Pratt School of Engineering and School of Medicine at Duke University. Y.H. acknowledges support from the NSF (grant no. CMMI 16-35443). This work was performed in part at the Duke University Shared Materials Instrumentation Facility, a member of the North Carolina Research Triangle Nanotechnology Network, which is supported by the National Science Foundation (award no. ECCS-2025064) as part of the National Nanotechnology Coordinated Infrastructure. Xiaoyue Ni thanks L. Bridgeman, J. Lu and Z. Wang for helpful discussions.

Author contributions Y.B., H.W., Y.H., J.A.R. and Xiaoyue Ni conceived the idea and designed the research. Y.B. and Y.Y. fabricated the samples. Y.B., Y.X., Y.P., J.-T.K., Xincheng Ni, T.-L.L., M.H. and Xiaoyue Ni performed the experiments. H.W. and Y.H. performed the finite-element modelling and theoretical study. Y.B. and Xiaoyue Ni analysed the experimental data. Y.B., H.W., Y.H., J.A.R. and Xiaoyue Ni wrote the manuscript, with input from all co-authors.

Competing interests The authors declare no competing interests.

Additional information

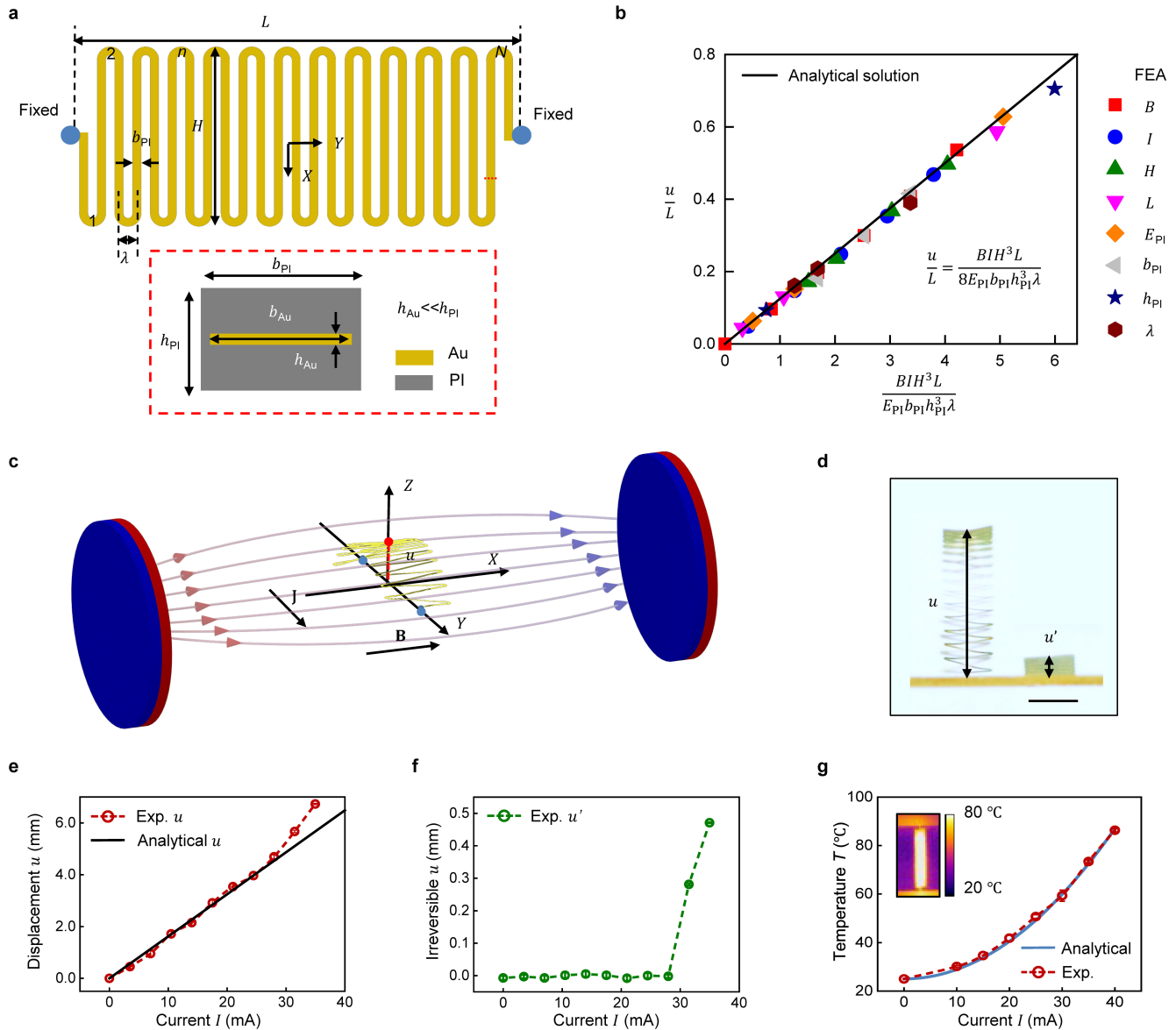
Supplementary information The online version contains supplementary material available at <https://doi.org/10.1038/s41586-022-05061-w>.

Correspondence and requests for materials should be addressed to Heling Wang, Yonggang Huang, John A. Rogers or Xiaoyue Ni.

Peer review information *Nature* thanks Guo Zhan Lum and the other, anonymous, reviewer(s) for their contribution to the peer review of this work. Peer reviewer reports are available.

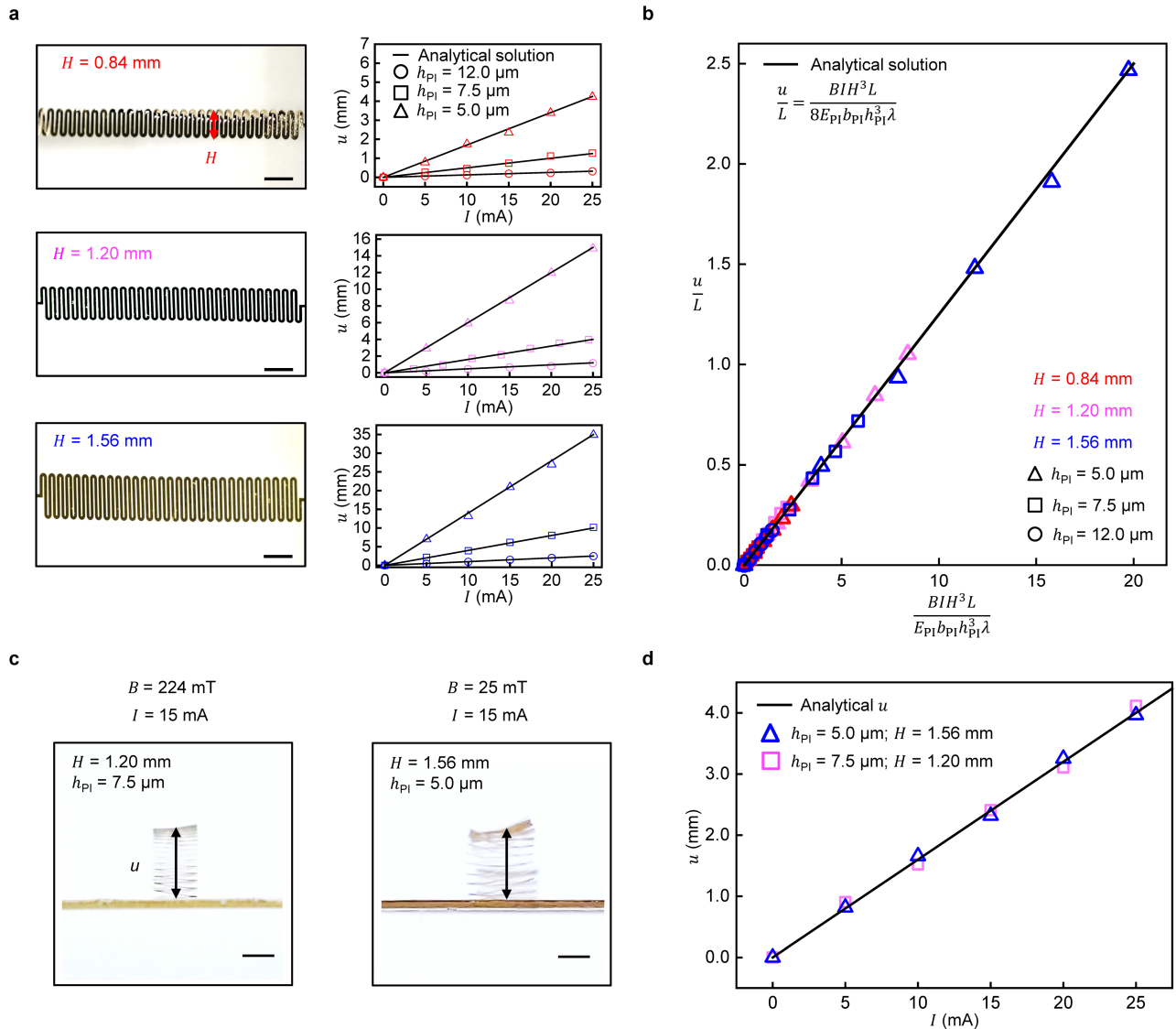
Reprints and permissions information is available at <http://www.nature.com/reprints>.

Article



Extended Data Fig. 1 | The analytical model of the electromagnetic response of a serpentine beam corroborated by FEA study and experimental characterizations. **a**, Schematic illustration (top and cross-sectional views) of the initial state of a serpentine beam (beam width $H=1.20$ mm, serpentine period $\lambda=0.18$ mm). **b**, Analytical model and FEA prediction of the maximum out-of-plane displacement u dependent on the combination of electric current I , magnetic field B , and material and geometry parameters. **c**, Schematic illustration of a single beam, placed in a magnetic

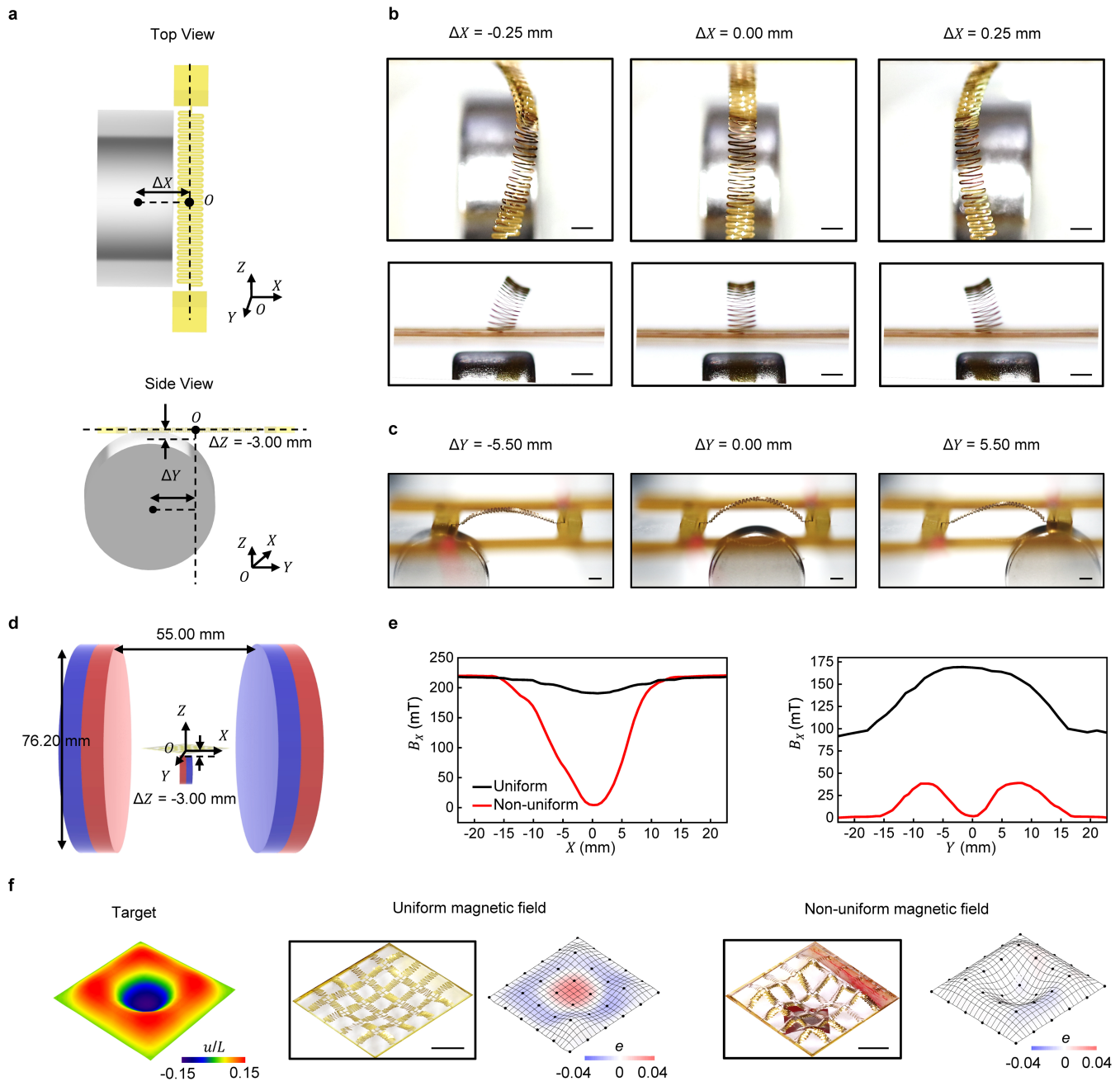
field \mathbf{B} and carrying a current density \mathbf{J} with an out-of-plane displacement u , under an electromagnetic force $\mathbf{F}_{\text{EM}}=\mathbf{J}\times\mathbf{B}$. **d**, Optical images of a representative serpentine beam (side view) driven to the maximum displacement u . If exceeding the elastic limit, an irreversible deformation u' will remain after unloading. **e–g**, Experimental characterizations of mechanical (e, f) and thermal (g) behaviors of a single beam under current-controlled electromagnetic actuation ($B=224$ mT) in comparison with the theoretical predictions. Scale bar, 1 mm.



Extended Data Fig. 2 | Experimental validation of the scaling law using a single serpentine beam. **a**, Top-view optical images of serpentine beams with the same beam length ($L = 11\text{ mm}$) but different beam widths ($H = 0.84\text{ mm}$, 1.20 mm , 1.56 mm). In a magnetic field of 224 mT , current-controlled experiments show that the electromagnetic responses of the beams with various PI thicknesses ($h_{\text{PI}} = 5.0\text{ }\mu\text{m}$, $7.5\text{ }\mu\text{m}$, $12.0\text{ }\mu\text{m}$) agree with the analytical solutions. **b**, Experimentally measured electromagnetic responses follow the scaling law

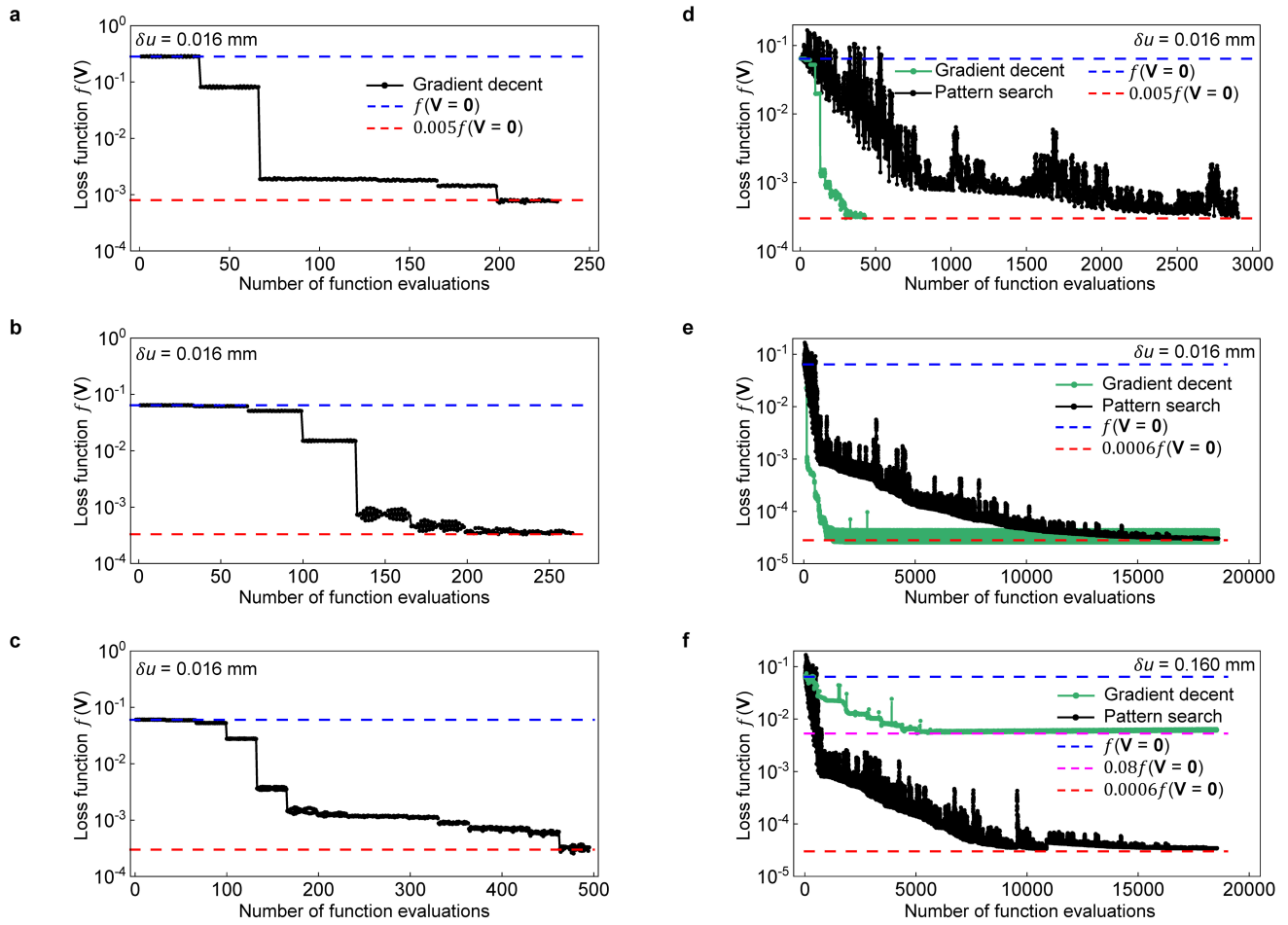
predicted by the analytical model. **c**, Side-view optical images of a serpentine beam of the design presented in the main text ($H = 1.20\text{ mm}$, $h_{\text{PI}} = 7.5\text{ }\mu\text{m}$) actuated in a magnetic field of 224 mT (left) and a tailored serpentine beam ($H = 1.56\text{ mm}$, $h_{\text{PI}} = 5.0\text{ }\mu\text{m}$) actuated in a reduced magnetic field of 25 mT (right). Applying the same current (15 mA) deforms the two beams to the same height (around 2.25 mm). **d**, The two beams in (c) exhibit approximately the same current-controlled mechanical behavior. Scale bars, 1 mm .

Article



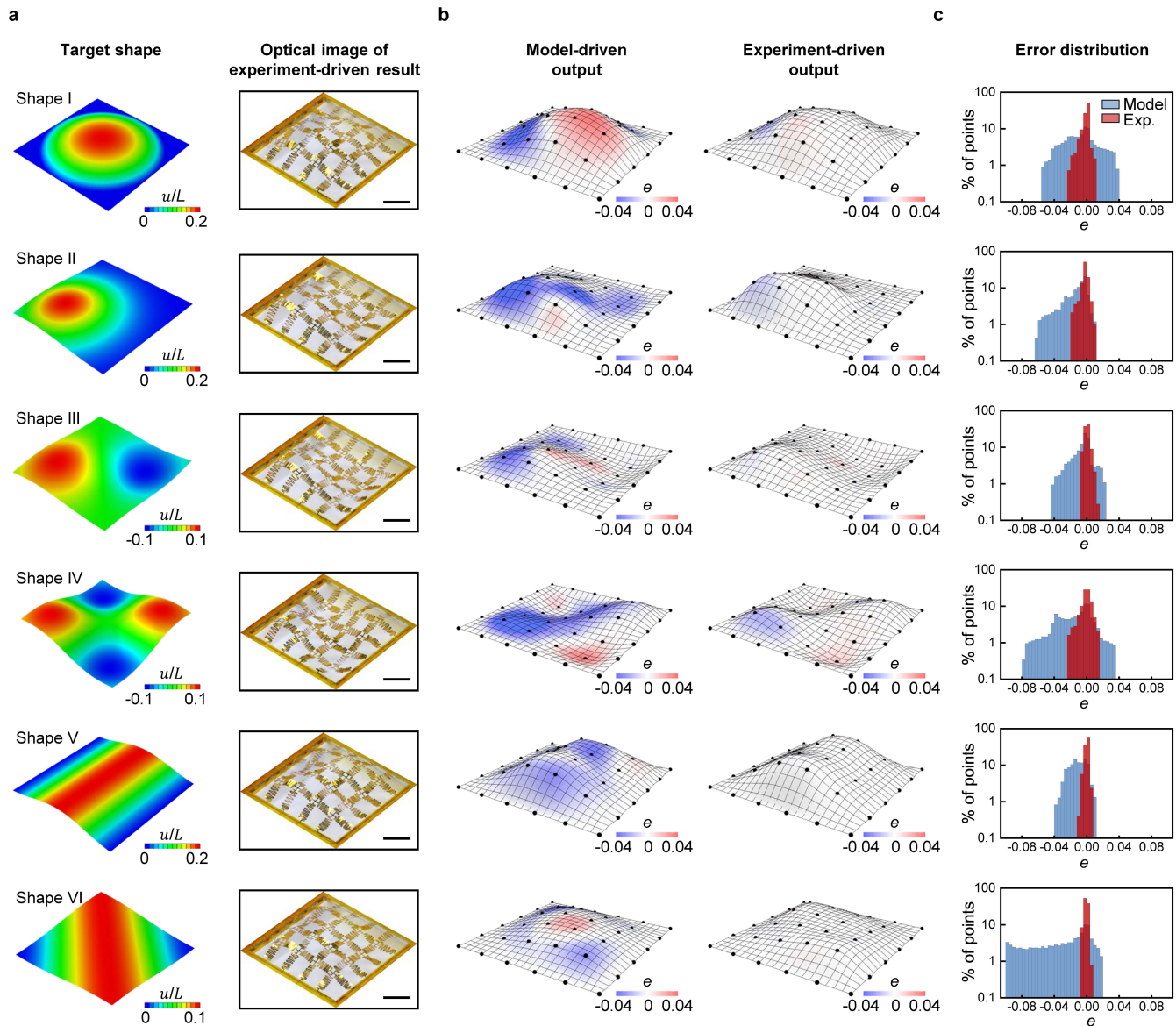
Extended Data Fig. 3 | Shape morphing in time-varying, non-uniform magnetic fields. **a**, Schematic illustration of a single serpentine beam in a non-uniform magnetic field generated by a small disk magnet (diameter $D = 11.0 \text{ mm}$, thickness $h = 5.0 \text{ mm}$, surface field $B = 481.6 \text{ mT}$) moving 3-mm below the beam ($\Delta Z = -3 \text{ mm}$). **b, c**, Optical images of the beam (applied current $I = 20 \text{ mA}$) changing shapes as the position of the magnet changes along X -axis (**b**, $\Delta Y = 0$) and Y -axis (**c**, $\Delta X = 0$). Scale bars, 1 mm. **d**, Schematic illustration of a 4×4 sample in a non-uniform magnetic field generated by a pair of large magnets ($D = 76.2 \text{ mm}$, $h = 12.7 \text{ mm}$, surface field $B = 245.1 \text{ mT}$) and a small

magnet ($D = 11.0 \text{ mm}$, $h = 5.0 \text{ mm}$, surface field $B = 481.6 \text{ mT}$) in the middle, 3.0 mm below the center of the sample. **e**, Magnetic flux density in X -direction (B_x) of the approximately uniform/non-uniform field measured by a gaussmeter (GMHT201, Apex Magnets) with/without the presence of the small magnet across the center (O) along X -axis (left) and Y -axis (right). **f**, Experimental results (optical images and 3D reconstructed surfaces) of a 4×4 sample morphing into the same donut-like target shape via the experiment-driven self-evolving process in the uniform and the non-uniform magnetic field. Scale bars, 5 mm.



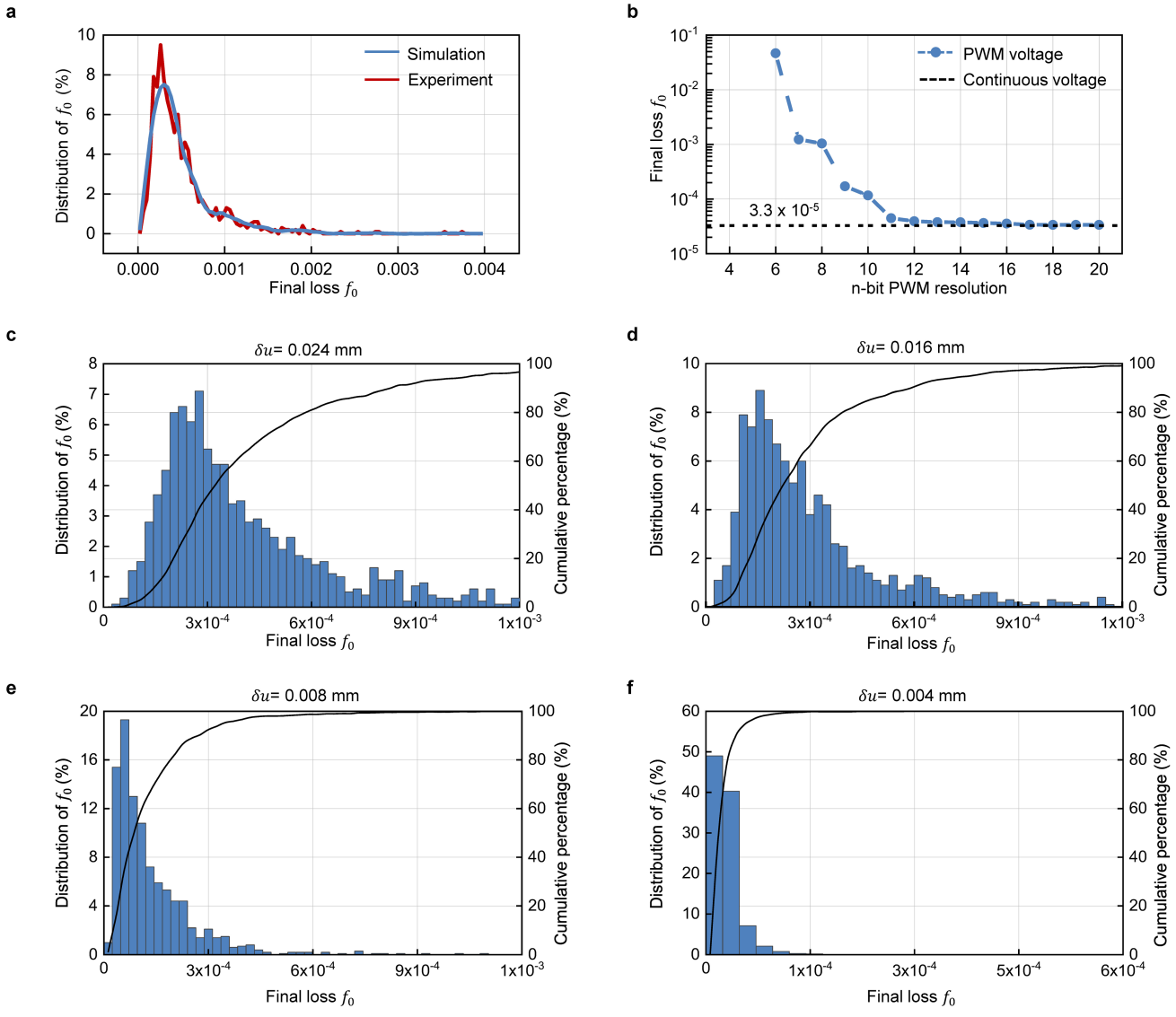
Extended Data Fig. 4 | Typical descent of loss function over function evaluations. **a–c**, For a 4×4 sample morphing into Shape I (a), III (b), IV (c) (Supplementary Note 8) through the experiment-driven approach using the gradient-based algorithm (see Methods section ‘Optimization algorithm’), the experimentally-measured loss function $f(\mathbf{V})$ (with an initial value $f(\mathbf{V} = \mathbf{0})$ in the range of 0.05–0.35) descends by ~99.5% to a steady state in 170–510 function evaluations (5–15 iterations). The 3D imaging noise is $\delta u = 0.016 \text{ mm}$ (Supplementary Note 14). **d–f**, Comparison of a global solver (pattern search algorithm) with the gradient-based algorithm for a 4×4 sample morphing into

Shape IV using model-driven simulation. Subjecting the objective function to typical experimental noise ($\delta u = 0.016 \text{ mm}$, Supplementary Note 14) and targeting a final loss of $0.005f(\mathbf{V} = \mathbf{0})$, the gradient-based algorithm finds the solution faster than the global solver (d). Both algorithms settle to a minimum loss of $0.0006f(\mathbf{V} = \mathbf{0})$ within 20,000 function evaluations (e). With pronounced noise ($\delta u = 0.16 \text{ mm}$), the gradient descent method ends up with a local solution ($0.08f(\mathbf{V} = \mathbf{0})$), while the pattern search method finds the same minimum ($0.0006f(\mathbf{V} = \mathbf{0})$) as the case with low noise (f).



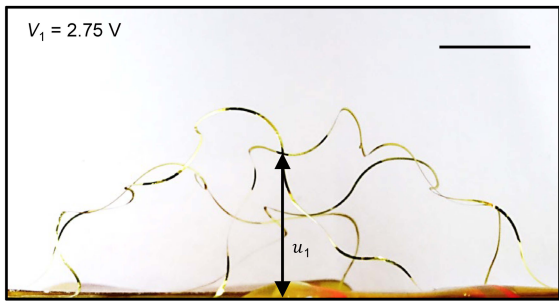
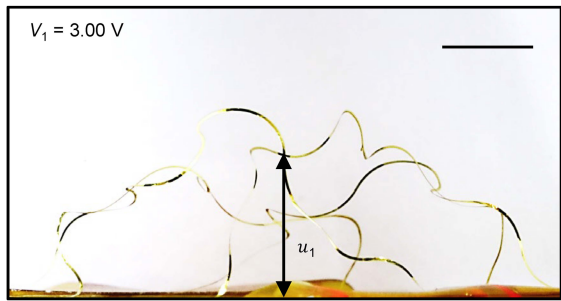
Extended Data Fig. 5 | Experiment-driven self-evolving process in comparison with the model-driven approach. **a**, Target explicit shapes and optical images of the experiment-driven morphing results of a 4×4 sample.

b, 3D reconstructed surfaces overlaid with contour plots of the minimized errors. **c**, Histogram plots of the minimized errors for model-driven and experiment-driven outputs. Scale bars, 5 mm.



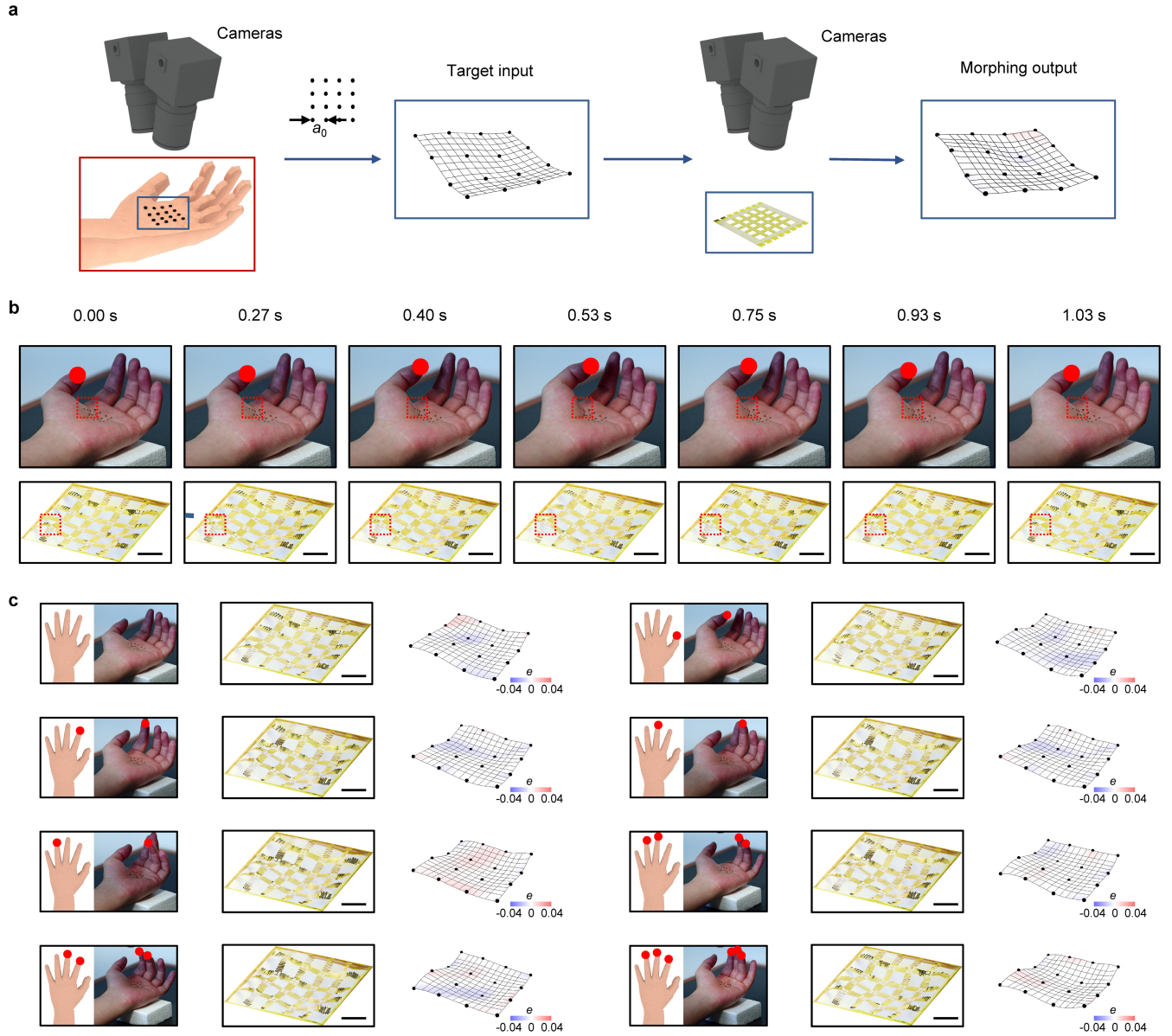
Extended Data Fig. 6 | Simulation of the impact of experimental noise on the optimization process. **a**, Comparison between the distribution of final loss f_0 after 15 iterations from model-driven simulations (1,000 trials, given 3D imaging noise $\delta u = 0.016 \text{ mm}$, 12-bit PWM output, and maximum current $I_{\max} = 27 \text{ mA}$) versus that from the experiments (97 trials), for a 4×4 sample morphing into the target shape in Fig. 3b. **b**, Simulation results of the final loss

f_0 (without imaging noise and iteration constraint) given n-bit PWM voltage control, compared with the case without actuation noise (continuous, analog voltage control). **c–f**, Histogram plots of the final loss f_0 (1,000 simulation trials) with a decreasing 3D imaging noise $\delta u = 0.024 \text{ mm}$ (c), 0.016 mm (d), 0.008 mm (e) and 0.004 mm (f).

a**b****c****d**

Extended Data Fig. 7 | The optical images of a 2×2 sample with modified serpentine design for amplified nonlinear mechanical behavior in response to a range of actuation voltages. **a–d**, Side-view images of the

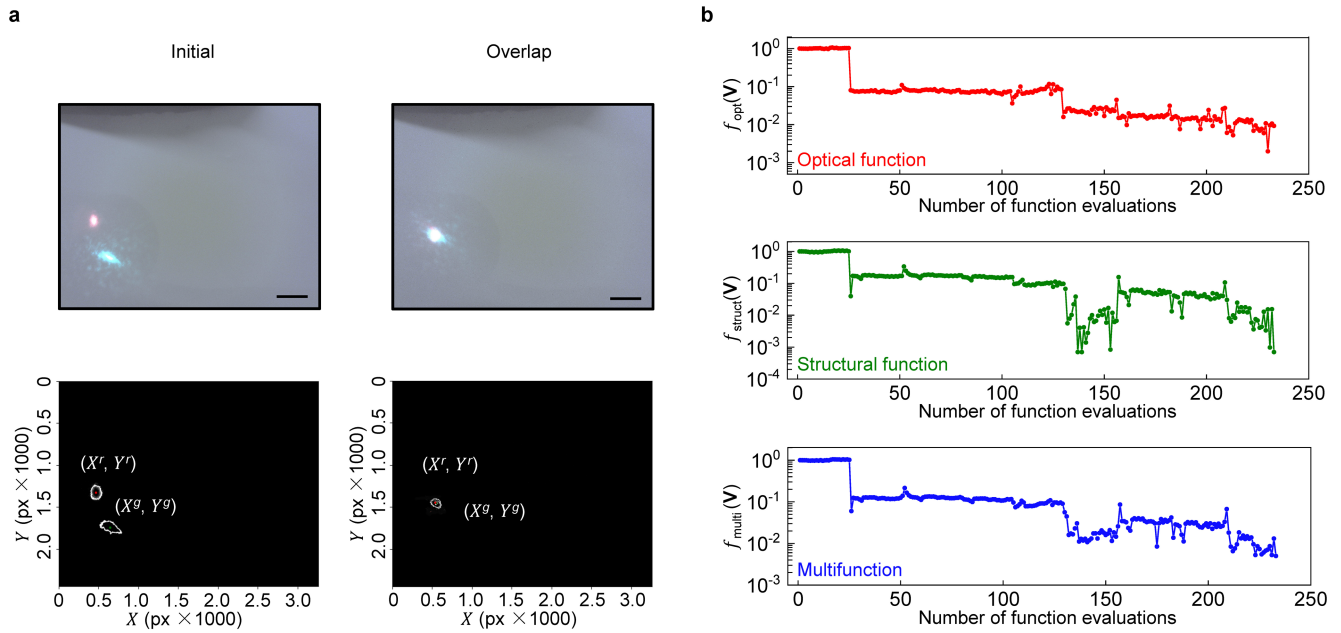
sample deforming out-of-plane given an increasing voltage to port 1 (Fig. 4a) given $V_1 = 0 \text{ V}$ (a), 0.25 V (b), 2.75 V (c), and 3 V (d), respectively. The rate of change of u_1 decreases as the actuation voltage increases. Scale bar, 5 mm.



Extended Data Fig. 8 | Self-evolving shape morphing toward semi-real-time shape learning. **a**, Schematic illustration of a duplicated stereo-imaging setup enabling a semi-real-time control of a 4×4 sample simulating the dynamic shape-shifting of a palm surface with 4×4 markers (with inter-spacing

$a_0 = 15 \text{ mm}$). **b**, Experimental results of the continuous semi-real-time shape learning of the palm surface with the thumb moving up. **c**, Morphing results of representative frames from a recording of hand making eight gestures. Scale bars, 5 mm.

Article

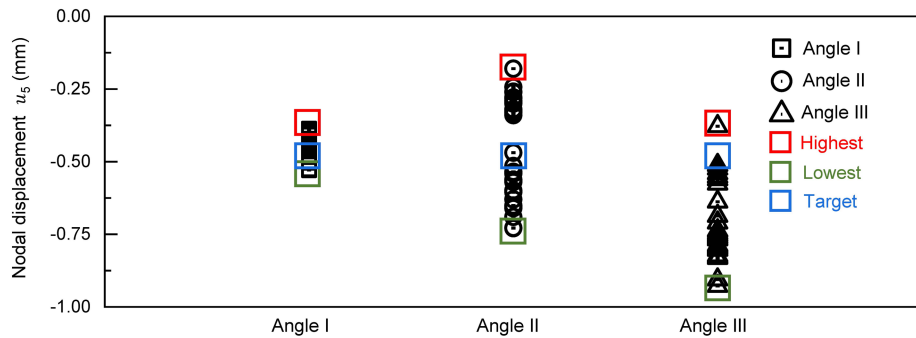


Extended Data Fig. 9 | A 3×3 reflective sample self-evolving to achieve an optical and a structural function simultaneously. **a**, Representative optical images of the laser spots on the receiving screen. The target optical function is to overlap two laser spots on the receiving screen. A customized image analysis method detects the centroid coordinates of the red/green laser spots to monitor their current locations on the screen ($[x^{rg}, y^{rg}]$). **b**, The typical

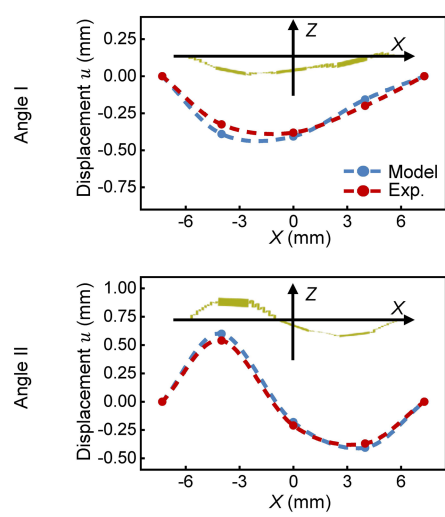
evolution of loss functions (Supplementary Note 16) over number of functional evaluations. The optimized loss function ($f_{\text{multi}}(V)$) is a linear combination of two parts: I) an optical loss function $f_{\text{opt}}(V)$ that evaluates the distance between the center of the two laser spots; II) a structural loss function $f_{\text{struct}}(V)$ that evaluates the central nodal displacement error. Scale bar, 5 mm.

a

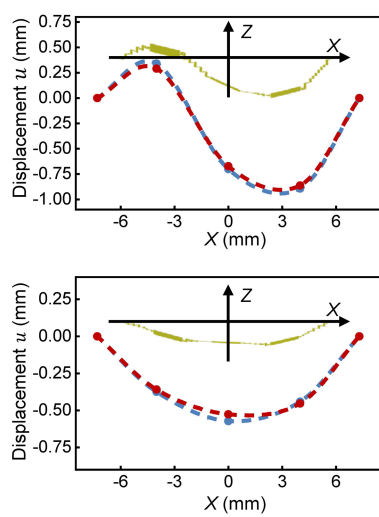
Solutions to overlap laser beams

**b**

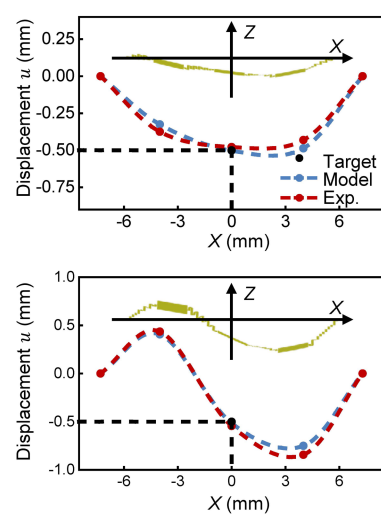
Highest displacement



Lowest displacement



Target displacement



Angle I

Angle II

Angle III

Extended Data Fig. 10 | Allowed shape (structural function) configurations of a 3×3 sample enforcing only the optical function (Fig. 5c, d). **a**, Allowed values of the central nodal displacement (u_5) when the sample overlaps the beams (when the distance between the centroids of the laser spots is less

than 0.1 mm) with three distinctive incident angles. **b**, Model predictions, and the ex-situ 3D imaging results of the sample (cross-sectional view) when overlapping the laser spots in the configurations with the highest, lowest, and target central displacement.